2D AND 3D NUMERICAL MODELS OF METAL CUTTING WITH DAMAGE EFFECTS

O. Pantalé, J.-L. Bacaria, O. Dalverny,
R. Rakotomalala and S. Caperaa

January 12, 2004

Laboratoire Génie de Production - Equipe C.M.A.O.
Ecole Nationale d'Ingénieurs de Tarbes (ENIT)
Avenue d'Azereix-BP 1629, 65016 Tarbes cedex France
Web page :http://www.enit.fr/lgp/cmao

Keywords: Metal cutting, Milling, Damage law, Finite elements, ALE.

Abstract

In this paper a two-dimensional and a three-dimensional finite element models of unsteady-state metal cutting are presented. These models take into account dynamic effects, thermo-mechanical coupling, constitutive damage law and contact with friction. The simulations concern the study of the unsteady-state process of chip formation. The yield stress is taken as a function of the strain, the strain rate and the temperature in order to reflect realistic behavior in metal cutting.

Unsteady-state process simulation needs a material separation criterion (chip criterion) and thus, many models in the literature use an arbitrary criterion based on the effective plastic strain, the strain energy density or the distance between nodes of parts and tool edge. The damage constitutive law adopted in models presented here allows defining advanced simulations of tool's penetration in workpiece and chip formation. The originality introduced here is that this damage law has been defined from tensile and torsion tests, and we applied it for machining process. Stresses and temperature distributions, chip formation and tool forces are shown at different stages of the cutting process.

Finally, we present a three-dimensional oblique model to simulate the unsteady-state process of chip formation. This model, using the damage law defined before, allows an advanced simulation close to the real cutting process. The final part shows a milling application.

An Arbitrary Lagrangian Eulerian formulation (ALE) is used for these simulations; this formalism combines both the advantages of Eulerian and Lagrangian representations in a single description, it is exploited to reduce finite element mesh distortions.

1 INTRODUCTION

Cutting is a very usefull way to obtain industrial pieces, but the deformation characteristics of machining processes are not well understood, and accurate models able to predict machining performances have yet to be improved. Precise knowledge about the optimal cutting parameters is essential. Process features such as tool geometry and cutting speed directly influence chip morphology, cutting forces, the final product dimensionality and tool life. Many investigators have now developed analytical and numerical models to gain a better understanding of the processes which involve deformation with large strains, strain rates and temperatures. Through finite element simulation, one is able to obtain various quantities numerically calculated such as the spatial distribution of stresses, strains, temperatures, but the main problem of those simulations is that we must

introduce the physics of the process through very accurate constitutive and contact laws. The second problem usually encountered is related to the kinematics of the process; the existing numerical models are usually based on updated Lagrangian or Eulerian formulations. In a Lagrangian model, the severe distortions of the finite element mesh affect the numerical solution of the problem; in addition, a separation criterion must be introduced to separate the chip from the workpiece. This one can either be a purely geometrical one [1] or a physical one [2]. Both can also be mixed together [3]. Using an Eulerian approach gives the opportunity to avoid the severe mesh distortions, but the problem here is that boundaries and geometry of the chip must be known previously.

Numerical models first appeared at the beginning of the seventies in the restricted case of orthogonal cutting; Eulerian models have been developed since 1980 [4, 5]. Many Lagrangian models [6, 7] have also been developed for the simulation of metal cutting. Generally, these models provide information about stresses and strain fields, shear zones, and temperature field when the model includes thermo-mechanical coupling. In 1985, Strenkowski and Carroll [8] have presented a thermo-mechanical model which predict residual stresses in the workpiece, as Shih et al. [1] in 1990. Lin and Pan [9], in 1993, have studied tool forces and compared with experiment. Sekhon and Chenot [2] in 1993, have also shown tool forces and stresses distribution. Other well-known authors as Marusich and Ortiz [10] and Obikawa et al. [3] have developed unsteady-state models applied to metal cutting. The difficulty in this kind of model is to determine the method allowing element and node separation and thus, chip formation. All of those models use a criterion to realize this operation. Often, this criterion of separation, generally called "chip criterion", is based on the strain energy density. A value of a critical distance is used by Shih et al. [1], between the tip of the cutting tool and the nodal point located immediately ahead. Obikawa et al. [3] have presented a model with a double-criterion based on the value of a critical plastic strain and a geometric criterion, thus they simulate fragmented chip formation. Sekhon and Chenot [2] use a plastic strain criterion. All of these criteria are generally arbitrary and are predefined on a nodal line corresponding to the trajectory of the tool tip. Most of them give good results close to the real cutting behavior. However, the use of this kind of chip criterion is arbitrary and generally applied in a localized zone where the contact will happen. Instead of using one of the separation criteria presented above, a damage law, as the material behavior law, will be used in our model to better represent the reality.

In this paper, we present a two-dimensional and three-dimensional finite element model of unsteady-state metal cutting. These models are able to simulate the formation of continuous and discontinuous chips during the process, depending on the material machined. Dynamic effects, thermo-mechanical coupling, constitutive damage law and contact friction are taken into account. The yield stress is taken as a function of the strain, the strain rate and the temperature. The damage constitutive law adopted here allows advanced simulations of tool penetration and chip formation. Stress and temperature fields, chip formation and tool forces are shown at different stages of the cutting process. Finally, we present a three dimensional simulation of a milling operation; it represents an extension of the model defined before.

The case of three dimensional orthogonal metal cutting has already been treated in the literature since the beginning of the nineties and notably by Lin and Lin [11] in 1999. The first three dimensional oblique models have been presented by Maekawa et al. [12] in 1990, Ueda and Manabe [13] in 1993 and Pantalé [14] in 1996. In the presented model we use the damage law already used previously, which provide interesting simulations.

The continuous and fragmented chip formation induce large mesh distortions and problems linked to the necessity to use a separation criterion to reduce numerical problems for these simulations. An Arbitrary Lagrangian Eulerian formulation (A.L.E.), already used by Rakotomalala [15], Pantalé [14] and Joyot [16], has been adopted in this work. The ALE approach has also been used recently by Olovsson et al. [17] in a two-dimensional finite element model of orthogonal metal cutting. This approach combines both the advantages of Eulerian and Lagrangian representations in a single description, and is exploited to reduce mesh distortions.

2 FINITE ELEMENT DISCRETIZATION

The Arbitrary Lagrangian Eulerian description is an extension of both classical Lagrangian and Eulerian ones. The grid points are not constrained to remain fixed in space (as in the Eulerian description) or to move with material points (as in Lagrangian description), but have their own motion governing equations. In such a

description, material points are represented by a set of Lagrangian coordinates $\overrightarrow{X}$, spatial points with a set of Eulerian coordinates $\overrightarrow{x}$ and reference points (grid points) with a set of Arbitrary coordinates $\overrightarrow{\xi}$ as shown in figure 1.

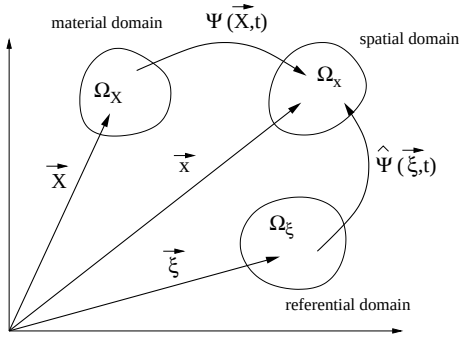

Figure 1: Motion description in A.L.E

At time t, a spatial point $\overrightarrow{x}$ is simultaneously the image of a material point $\overrightarrow{X}$ by the material motion $\overrightarrow{x} = \Psi(\overrightarrow{X}, t)$, and the image of a reference point $\overrightarrow{\xi}$ by the grid motion $\overrightarrow{x} = \widehat{\Psi}(\overrightarrow{\xi}, t)$.

The material velocity $\overrightarrow{v}$ of the particles is obtained using a classical material $\overset{\bullet}{()}$ derivative, while the grid velocity $\overrightarrow{\hat{v}}$ is obtained after the introduction of a mixed $\overset{\circ}{()}$ derivative (see Pantalé et al. [18] for further details) which must be interpreted as the "time" variation of a physical quantity for a given grid point.

$$\overrightarrow{v} = \overset{\bullet}{\overrightarrow{x}} = \left.\frac{\partial \overrightarrow{x}}{\partial t}\right|_{\overrightarrow{X}=cte} \quad and \quad \overrightarrow{\hat{v}} = \overset{\circ}{\overrightarrow{x}} = \left.\frac{\partial \overrightarrow{x}}{\partial t}\right|_{\overrightarrow{\xi}=cte} \tag{1}$$

All physical quantities are computed at spatial points $\overrightarrow{x}$ at time t. All conservation laws must be expressed taking into account the grid motion during the simulation.

2.1 Conservation laws in ALE description

We will use conservation laws in a form almost identical to those of the Eulerian description. According to the following relation $\overset{\bullet}{()} = \overset{\circ}{()} + \overrightarrow{c}\nabla()$ where $\overrightarrow{c} = \overrightarrow{v} - \overrightarrow{\hat{v}}$ is the so-called convective velocity and ∇ is the gradient operator, all Eulerian conservation laws (mass, momentum and energy) can be re-written according to the ALE description as following:

$$\overset{\circ}{\rho} + \overrightarrow{c}\nabla\rho + \rho \mathrm{div}\,\overrightarrow{v} = 0 \tag{2}$$

$$\rho\,\overset{\circ}{\overrightarrow{v}} + \rho\overrightarrow{c}\nabla\overrightarrow{v} = \overrightarrow{f} + \mathrm{div}\sigma \tag{3}$$

$$\rho\,\overset{\circ}{e} + \rho\overrightarrow{c}\nabla e = \sigma : \mathbf{D} - \mathrm{div}\,\overrightarrow{q} + r \tag{4}$$

where ρ is the mass density, $\overrightarrow{f}$ are the body forces, σ is the Cauchy stress tensor, e is the specific internal energy, $\mathbf{D}$ is the strain rate tensor, r is the body heat generation and $\overrightarrow{q}$ is the heat flux vector. In such a description, the ALE form may be considered as an automatic and continuous re-zoning method.

2.2 Spatial discretization

In finite element approximation, we define all dependent variables as functions of element coordinates. The ALE domain is subdivided into elements and for element e, the ALE coordinates are given by $\xi = \xi_I N_I$ where

N are the geometrical shape functions of element e. In view of spatial discretization of the mass, momentum and energy equations (2), (3) and (4) by the finite element method, a classic variational form is obtained by multiplying these equations respectively by a set of weighting function ($\overset{\circ}{\rho}^*$, $\overset{\circ}{v_i}^*$, $\overset{\circ}{e}^*$) over the spatial domain R_x. Employing the divergence theorem, the variational forms associated with these equations, and finally, using the Galerkin approach, one obtain the corresponding discretized equations:

$$M^\rho \overset{\circ}{\rho} + L^\rho \rho + K^\rho \rho = 0 \tag{5}$$

$$M^v \overset{\circ}{v} + L^v v + f^{int} = f^{ext} \tag{6}$$

$$M^e \overset{\circ}{e} + L^e e = r \tag{7}$$

where M^ρ, M^v, M^e are the generalized mass matrices for the corresponding variables in (5), (6) and (7), respectively; L^ρ, L^v, L^e are the generalized convective matrices; K^ρ is the stiffness matrix for density; f^{int} is the internal force vector; f^{ext} is the external load vector; r is the generalized energy source vector. As an example, we present here-after the expression of those matrices and vectors for the momentum equation:

$$M^v = \mathbf{I}\left[M^v_{IJ}\right] = \left(\int_{R_x} \rho \overline{N}^v_I N^v_J dR_x\right)\mathbf{I} \tag{8}$$

$$L^v = \mathbf{I}\left[L^v_{IJ}\right] = \left(\int_{R_x} \rho \overline{N}^v_I c_i N^v_{J,j} dR_x\right)\mathbf{I} \tag{9}$$

$$f^{int} = f^{int}_{iI} = \int_{R_x} \overline{N}^v_{I,j}\sigma_{ij} dR_x \tag{10}$$

$$f^{ext} = f^{ext}_{iI} = \int_{R_x} \overline{N}^v_I b_i dR_x + \int_{\delta R_x} \overline{N}^v_I t_i d\delta R_x \tag{11}$$

where N^v and $\overline{N}^v$ are the shape functions and the test shape functions for the velocity, b_i is the body force vector, t_i is the traction on the surface vector (including contact forces). The internal and external force vectors are identical to those of the updated Lagrangian formulation except that they are expressed in terms of the test shape functions. The mass matrix is not constant in time since the density and the domain vary with time. This one therefore has to be computed for each time-step.

Four nodes quadrilateral elements with a reduced integration scheme have been used for the discretization of the problem in 2D simulations while 8 nodes brick elements with also a reduced integration scheme are used in 3D.

2.3 Explicit dynamic analysis

The equations of motion for the body are integrated using the explicit central difference integration rule.

$$v^{(i+\frac{1}{2})} = v^{(i-\frac{1}{2})} + \frac{\Delta t^{(i+1)} - \Delta t^i}{2}\overset{\bullet}{v}^{(i)} \tag{12}$$

where v is the velocity and $\overset{\bullet}{v}$ the acceleration, the superscript (i) refers to the increment number and $(i-1/2)$ and $(i+1/2)$ refer to mid-increment values. The central difference integration operator is explicit in the sense that the kinematic state can be obtained using known values of $v^{(i-1/2)}$ and $\overset{\bullet}{v}^{(i)}$ from the previous increment. The explicit integration scheme is quite simple but by itself does not provide the computational efficiency associated with the explicit dynamics procedure. The key to the computational efficiency is the use of diagonal mass matrices because the inversion of the mass matrix used in the computation of the accelerations vector is trivial:

$$\overset{\bullet}{v}^{(i)} = M^{-1}\left(f^{ext^{(i)}} - f^{int^{(i)}}\right) \tag{13}$$

where M is the lumped mass matrix, $f^{ext^{(i)}}$ is the external force vector, $f^{int^{(i)}}$ is the internal force vector. The explicit procedure requires no iterations and no tangent stiffness matrix. Hughes [19] showed that the use of an appropriate lumped mass matrix gives very accurate results and a significant reduction of the simulation cost. But the price to pay for this simplicity is that this integration scheme is conditionally stable in time. In fact the explicit procedure integrates the time by using very small time increments. A stable time increment is computed for each element in the mesh. A conservative estimate of the stable time increment is given by the minimum taken over all the elements. The critical time-step for a mesh of constant strain elements with rate-independant materials is given by:

$$\Delta t = \alpha \Delta t_{crit} \quad \Delta t_{crit} \leq \min_{e}(\frac{L_e}{c_e}) \tag{14}$$

where L_e is the characteristic length of the element and c_e is the current wave-speed in the element and α is a reduction factor that accounts for the destabilizing effects of the non-linearities. A good choice of α is $0.8 \leq \alpha \leq 0.98$. The above is the so-called Courant stability condition.

In this work, the ALE approach introduces advective terms into the conservative equations to account for independent mesh and material motions. There are two basic ways to solve these modified equations: solve the non-symmetric system of equations directly, or decouple the Lagrangian (material) motion from the additional mesh motion using an operator split. Furthermore, this technique is appropriate in an explicit setting because small time increments limit the amount of motion within a single increment. For a time step, the solution is advanced according the following procedure:

- A Lagrangian step is performed. The displacements are computed using the explicit integration scheme described previously, and all internal variables are updated.
- Then a mesh motion step is performed to move the nodes in order to reduce element distortions. All states variables are therefore transported in the advection part of the procedure.

We will not present more the classical Lagrangian step but will focus on the mesh motion and advection steps necessary according to the ALE description.

2.4 Mesh update procedure

Following the Lagrangian step, a mesh update procedure is used to move the grid nodes according to various algorithms. The node motion procedure is based on three algorithms, the volume smoothing, the Laplacian smoothing and the equipotential smoothing. To choose the method to use or to combine the smoothing methods, the user have to specify a weighting factor for each method in the range $[0, 1]$. The sum of those three factors should typically be 1.0. The smoothing methods are applied to each node of the ALE domain in order to determine the new location of the node based on the location of the surrounding nodes or elements.

According to the volume smoothing procedure, each node is relocated by computing a volume weighted average of the element centers in the elements surrounding the considered node as illustrated in figure 2. This so called Kikuchi's algorithm is iterative and the relocation of the nth node (node M in figure 2) at the $(i+1)$th iteration is given by the following equation:

$$x_n^{i+1} = \frac{\sum_{e=1}^{nsel} V_e^i x_e^i}{\sum_{e=1}^{nsel} V_e^i} \tag{15}$$

where x_n^{i+1} is the new position of the node M, V_e^i is the volume of the surrounding eth element, x_e^i is the position of the center of the eth element and $nsel$ is the number of surrounding elements of node M. The volume smoothing procedure will tend to push the node away from element center x_e^1 toward to element center x_e^3, thus reducing element distortion. Volume smoothing is very robust and is the default procedure used in this work.

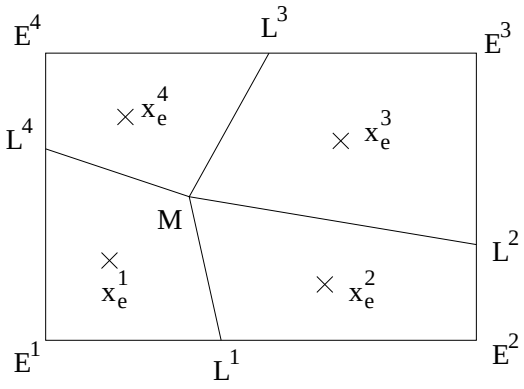

Figure 2: Node relocation

Laplacian smoothing relocates a node by calculating the average of the position of each of the adjacent nodes connected by an element edge to the node in question. In figure 2 the new position of the node M is therefore determined by the average position of the four nodes L^i connected to node M by element edges. This will pull node M right to reduce element distortion. This is the least expensive algorithm usually used in mesh preprocessors. For low to moderately distorted mesh domains, the results of Laplacian smoothing is similar to volume smoothing.

Equipotential smoothing is a high-order weighted average method that relocates a node from the positions of the node's height nearest neighbor nodes in two-dimensions or eighteen nearest neighbor nodes in three-dimensions. In figure 2 the position of node M is based on the position of all surrounding nodes L^i and E^i. This one is fairly complex and is based on the solution of the Laplace equation. This one tends to minimize the local curvature of lines running across a mesh over several elements.

2.5 Advection step

Element and material variables must be transferred from the old mesh to the new mesh in each advection step. The vast majority of algorithms employed in such case were originally developed by the computational fluid mechanics community [20]. The method used in this work for the advection of the element variables is the so called second-order method based on the work of Van Leer [21]. An element variable ϕ is remapped from the old mesh (at the instant n) to the new mesh (at the instant $n+1$) by first determining a linear distribution of the variable ϕ in each old element. The mapping procedure must guarantee the state variable conservation during the mesh motion. Therefore, each state variable must remain unchanged during the advection step:

$$\frac{\mathrm{D}\phi}{\mathrm{D}t} = \frac{\partial \phi}{\partial t} + \widehat{v}_i \frac{\partial \phi}{\partial x_i} = 0 \tag{16}$$

The method is briefly described in the following section, but for reasons of clarity, we present it here for one dimension.

$$\frac{\partial \phi}{\partial t} + \hat{v} \frac{\partial \phi}{\partial x} = 0 \tag{17}$$

Using the finite difference notation, the equation (17) is solved by means of the following upwind scheme:

$$\phi_{j+\frac{1}{2}}^{n+1} = \phi_{j+\frac{1}{2}}^{n} + \frac{\Delta t}{\Delta x} \left(\psi_j - \psi_{j+1} \right) \tag{18}$$

$$\psi_j = \frac{\hat{v_j}}{2} \left(\phi_{j-\frac{1}{2}}^{n} + \phi_{j+\frac{1}{2}}^{n} \right) + \frac{|\hat{v_j}|}{2} \left(\phi_{j-\frac{1}{2}}^{n} - \phi_{j+\frac{1}{2}}^{n} \right) \tag{19}$$

where $\phi^n_{j+\frac{1}{2}}$ is the average value at the instant n over the interval $[x_j, x_{j+1}]$ of a non constant linear distribution $\phi^n(x)$.This linear distribution of $\phi^n(x)$ in the middle element depends on the values of ϕ^n in the two adjacent elements. To construct this linear distribution:

- A quadratic interpolation is constructed from the constant values of ϕ^n at the integration points of the middle element and its adjacent elements.
- A trial linear distribution ϕ^n_{trial} is found by differentiating the quadratic function to find the slope at the integration point of the middle element.
- Then the trial linear distribution in the middle element is limited by reducing its slope until its minimum and maximum are in the range of the original constant values in the adjacent elements. This process referred to as flux-limited is necessary to ensure that the advection is monotonic.

Once the flux-limited linear distributions are determined for all elements of the old mesh, these distributions are evaluated over each new element.

Concerning the momentum equation, nodal velocities are computed on the new mesh by first advecting momentum, then using the mass distribution on the new mesh to calculate velocity field. The half-index shift method [22] is used for advecting the momentum equation.

3 CONSTITUTIVE AND CONTACT LAWS

3.1 Material constitutive law

The original form of the Johnson-Cook [23] material law is used for the simulations presented in this paper. This relationship is frequently adopted for dynamic problems with high strain rates and temperature effects. Assuming a von Mises type yield criterion and an isotropic strain hardening rule, the yield limit is given by:

$$\sigma = \left(A + B\overline{\varepsilon^p}^n\right)\left(1 + C\ln\frac{\dot{\overline{\varepsilon^p}}}{\dot{\overline{\varepsilon}}_0}\right)\left[1 - \left(\frac{T - T_0}{T_{melt} - T_0}\right)^m\right] \tag{20}$$

where $\overline{\varepsilon^p}$ is the equivalent plastic strain, $\dot{\overline{\varepsilon^p}}$ the equivalent plastic strain rate, T the temperature, and A, B, C, m, n, T_0, T_{melt}, $\dot{\overline{\varepsilon}}_0$ are material parameters.

For the determination of these material parameters we developed specific experimental tests coupled to numerical modelings. In our application we used the classical "symmetric Taylor impact test", where target and projectile are identical. The impacted end usually sustains a large amount of plastic deformation and the final shape has been used to estimate the dynamic material properties of the projectile.

Experiments are done using the compressed gas gun facility shown in the left side in figure 3. The impact speed ranges from 100 to 350 m/s, specimens are initially 10 mm diameter and 28 mm length.

The evaluation is based on a comparison of computed and experimentally measured final deformed shapes. The experimental deformed shape is measured using a macro-photographic device. Comparisons between this process and a standard three dimensional device has leaded to a relative error less than 0.5%, providing a precision of 0.01 mm.

The numerical model performed with the Abaqus/Explicit [24] finite element code, uses four node, axi-symmetric solid elements with reduced integration. Right side in figure 3 shows the initial mesh and an example of the final step.

For the identification, we use a procedure based on a combination of a Monte-Carlo (for the coarse research) and Levenberg-Marquardt (for the refined research) algorithms [25]. The experimental responses concern the

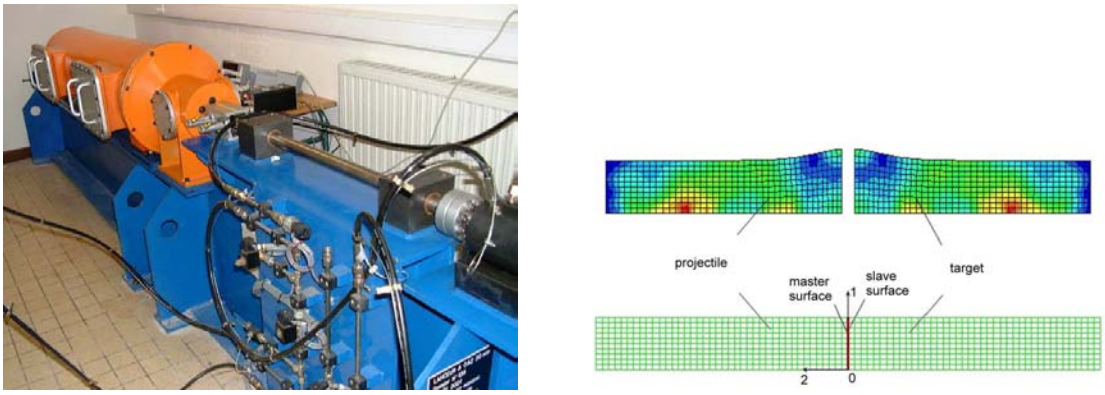

(a) (b)

Figure 3: Impact apparatus and numerical model of the test

final length, the radius of the deformed end, and few other intermediate radii depending on user choice. The objective function to be minimized by the optimization procedure presents the following form:

$$f = \frac{1}{m}\sqrt{\sum_{j=1}^{m} w_r[j]\left(\frac{r_{EF}[j] - r_{EXP}[j]}{r_{EXP}[j]}\right)^2} \tag{21}$$

where m is the total number of responses, r_{EF} is the vector of the simulated responses, r_{EXP} is the vector of the experimental responses and w_r is the vector of the responses weights. This algorithm has been implemented using the C++ language, Python scripts are used to pilot the Abaqus/Explicit code. This procedure has been applied to a 42CrMo4 steel. Results are reported in table 1.

A	$595\,MPa$
B	$580\,MPa$
C	0.023
n	0.133
m	1.03
T_{melt}	$1793°K$
T_0	$3003°K$

Table 1: Johnson-Cook material law parameters for the 42CrMo4

3.2 Damage law

The use of a damage law is necessary to simulate unsteady-state metal cutting. As mentioned above, we decided not to include a simple arbitrary chip separation criterion; a damage law depending on material characteristics represents a better way.

Johnson and Cook have developed a damage law [26] which takes into account strain, strain-rate, temperature, and pressure. The originality is that this law has been defined from tensile and torsion tests. The damage

is calculated for each element and is defined by:

$$D = \sum \frac{\Delta \overline{\varepsilon^p}}{\overline{\varepsilon^p}^f} \tag{22}$$

where $\Delta \overline{\varepsilon^p}$ is the increment of equivalent plastic strain during an integration step, and $\overline{\varepsilon^p}^f$ is the equivalent strain to fracture, under the current conditions. Fracture is then allowed to occur when $D = 1.0$ and the concerned elements are removed from the computation. In fact, they still exist, in order to keep the number of nodes, elements and connectivities between nodes constant (important for the simplicity of the ALE algorithm), but the deviatoric stress of the corresponding element are set to zero and remains zero for the rest of the analysis. The general expression for the fracture strain is given by:

$$\overline{\varepsilon^p}^f = (D_1 + D_2 \exp D_3 \sigma^*) \left(1 + D_4 \ln \frac{\dot{\overline{\varepsilon^p}}}{\dot{\overline{\varepsilon}}_0}\right) \left[1 - D_5 \left(\frac{T - T_0}{T_{melt} - T_0}\right)^m\right] \tag{23}$$

depending on the variables $(\sigma^*, \dot{\overline{\varepsilon^p}}, T)$. The dimensionless pressure-stress ratio is defined as $\sigma^* = \frac{\sigma_m}{\overline{\sigma}}$ where σ_m is the average of the three normal stresses and $\overline{\sigma}$ is the von Mises equivalent stress.

The expression in the first set of brackets of equation (23) follows the form presented by Hancock and Mackenzie [27] and essentially indicates the decrease in strain fracture as the hydrostatic pressure (σ_m) increases and the yield stress decreases. From numerical simulations we noticed that the influence of D_4 and D_5 have no major influence in cutting context.

The constants of the Johnson-Cook fracture criterion D_1, D_2 and D_3 are identified from tensile tests [26]. The tensile tests were carried out in our laboratory on a tensile test machine with notched specimens with different radius curvatures. Two CCD cameras and the Aramis 3D [28] software have also been used to measure displacement fields in the cracked zone and to deduce strain fields (see figures 4 and 5).

The measurements obtained, after the tensile test of each specimen, enable the determination of the equivalent plastic strain at rupture. Pairs of values obtained $(\sigma^*, \overline{\varepsilon^p}^f)$ are shown in the graph, (see right side in figure 5). The material parameters D_i are obtained by using the same procedure as for the constitutive law. D_4 and D_5 are determined by tensile and torsion tests. The used values for the 42CrMo4 steel are reported in table 2.

D_1	1.5
D_2	3.44
D_3	-2.12
D_4	0.002
D_5	0.1

Table 2: Fracture parameters for the 42CrMo4 steel

These material parameters will now be used for the metal cutting simulations.

3.3 Contact law

In a metal cutting process, due to of high stresses, high strain rates and high temperatures, a high mechanical power is dissipated in the tool-chip interface thus leading to many structural modifications of the contacting pieces. Therefore, Shih et al. [29] shows that no universal contact law exists which can predict friction forces among a wide range of cutting conditions. Childs et al. [6] show that stick and slip zones along the inter-facial zone between the chip and the tool depend on cutting conditions, pressure, temperature, etc...

In our model, a classical Coulomb friction law is assumed to model the tool-chip and the tool-workpiece contact zones. The contacting bodies will be assumed sticked together if $\|T_t\| < \mu |T_n|$ and in a relative motion

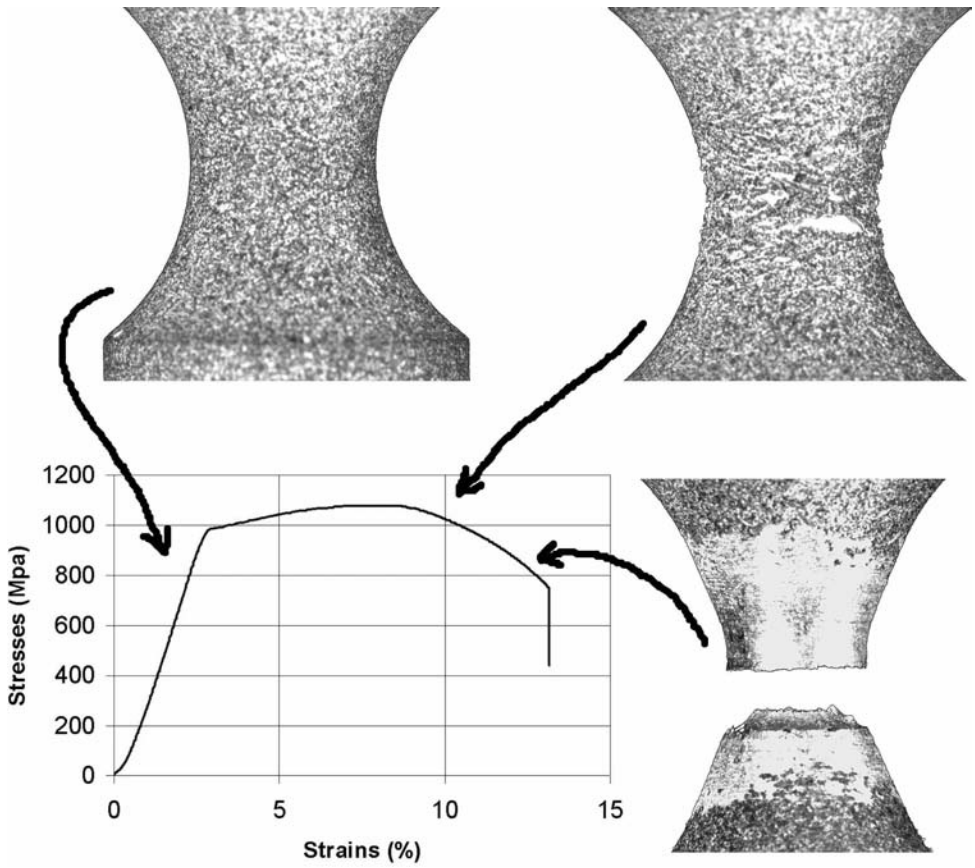

Figure 4: CCD pictures at different steps of the tensile test

if $\|T_t\| = \mu |T_n|$ with T_n and T_t representing the normal and tangential components of the surface traction at the interface and μ the friction coefficient assumed as a constant depending on the nature of the contacting bodies. A value of $\mu = 0.32$ is assumed, this one has been determined from a specific friction test [16].

4 NUMERICAL RESULTS AND VALIDATION

While metal cutting is one of the most frequent operation in manufacturing today, a general predictive model of the cutting process is not yet available. The reason is that the physical phenomena associated with the process are extremely complex: friction, adiabatic shear bands, free surfaces, heating, large strains and strain rates.

The model of unsteady chip formation presented here tries to take into account most of these physical phenomena. The tool is considered to be rigid. The cutting parameters (cutting speed V_c, depth of cut S, width of cut W) for the turning process in figure 6a are given in table 3. These are real values corresponding to the physical process.

Those parameter values will allow experimental [16] and numerical [14] comparisons. The length of workpiece in numerical simulations is $10\,mm$, the height is $5\,mm$ and the thickness is $2\,mm$ (this is important for cutting forces comparisons further). The rigid cutting tool (see figure 6b) has a rake angle equal to $5.7°$ as his flank angle and the radius of the cutting edge is equal to $0.1\,mm$. The initial temperature of the workpiece is assumed to be $300°K$. The workpiece is fixed in space to his base, and we only move the tool. Furthermore, we will refer

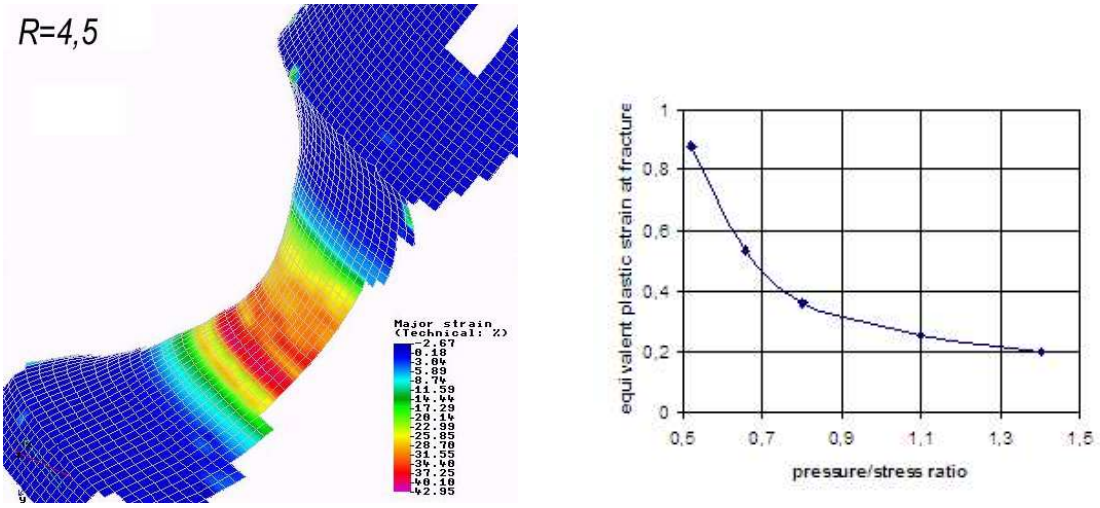

Figure 5: Strain fields for a specimen with a radius curvature of $R = 4.5mm$ and results for the 42CrMo4 steel

Material	42CrMo4
V_c	$4\,m/s$
S	$0.5\,mm$
W	$2\,mm$

Table 3: Cutting parameters for turning operation

to the first and secondary shear bands (see figure 6c) for the localization of those zones.

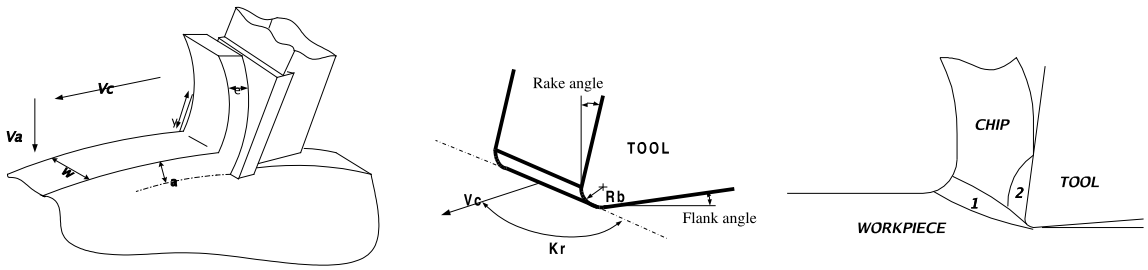

(a) turning process

(b) tool description

(c) primary and secondary shear bands

Figure 6: Description of the cutting process

All numerical computations in this work were run with Abaqus v. 5.8 on an Hewlett-Packard J6000 workstation with 1Gb of core storage under HP.UX 11.0. Details concerning the sizes of the numerical models, the computation durations are given further for each example. Many other tests have been conducted for this work, and we only present three major ones.

4.1 Two-dimensional model results

The first numerical example concerns the so-called orthogonal transient turning process ($K_r = 90°$). The numerical model is made of 5149 nodes and 5006 plane strain elements.

The simulation shows the tool penetration and the formation of the continuous chip. Figure 7 shows von Mises stress fields at different stages of the simulation and an example of temperature field. The cutting force, during the simulation, is represented in figure 8. Finally, we have choosen a point in the center of the first shear band of the chip to obtain plastic strain evolution (see figure 8). This point, forced to stay at a given distance of the tool tip, is used here to detect the time needed to reach the steady-state part of the cutting process. Caution should be given to right side of figure 8 since this point is linked to the tool motion and is not a material point. Plastic strain increases rapidly during the penetration of the tool into the workpiece then the value slightly decrease and stabilizes during the process.

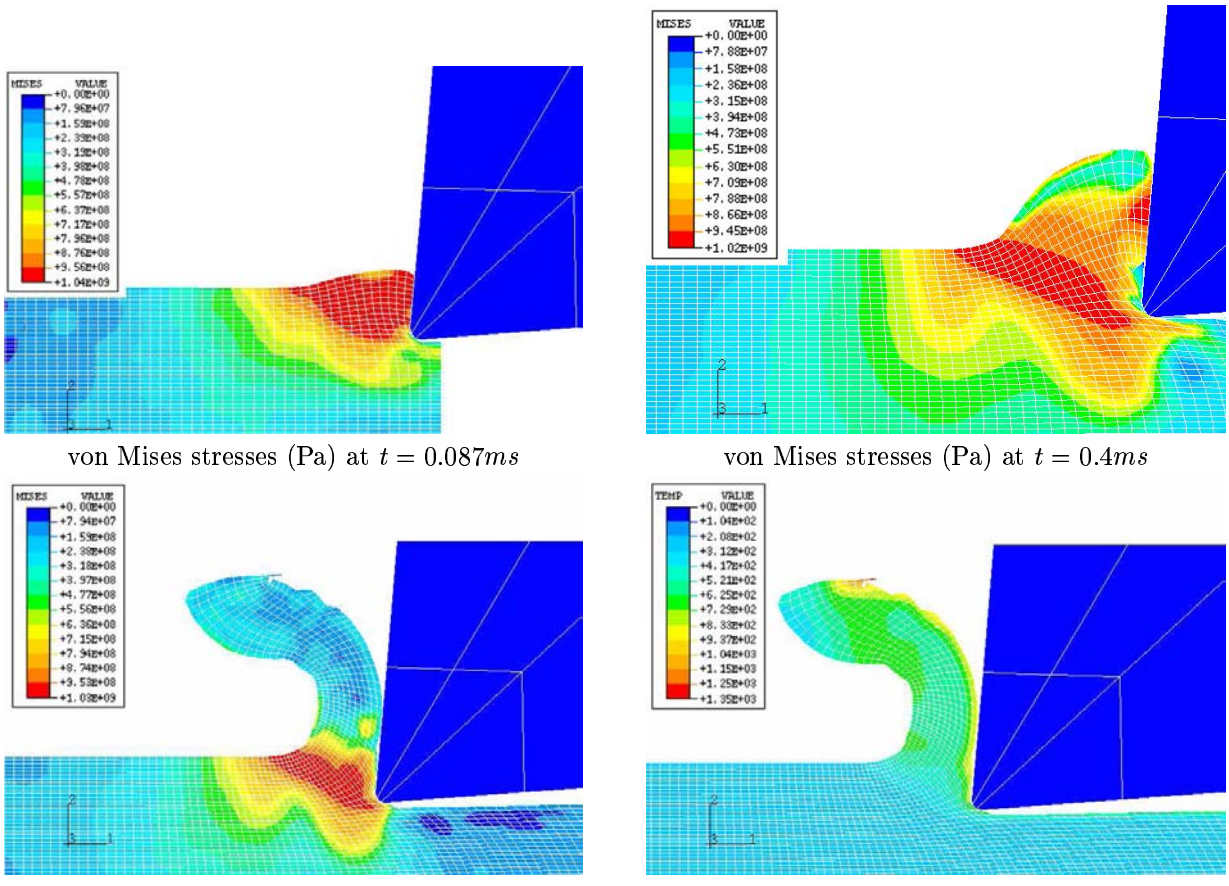

von Mises stresses (Pa) at $t = 0.087ms$

von Mises stresses (Pa) at $t = 0.4ms$

von Mises stresses (Pa) at $t = 1.3ms$

temperature field (Kelvin) at $t = 1.3ms$

Figure 7: Chip formation and field variables at different times

These simulations illustrate the tool penetration in the workpiece and the chip formation. In agreement with experiments [14] the chip is a continuous one due to material and cutting conditions choosen. It has been established that the maximum value of von Mises stress occurs over the primary shear band [14]. Temperature field shows the maximum value in the contact area between the tool rake face and the chip, due to a secondary shear band effect.

When the chip geometry is stable, cutting force reaches a value of $1800N$ ($900N/mm$, remembering that the

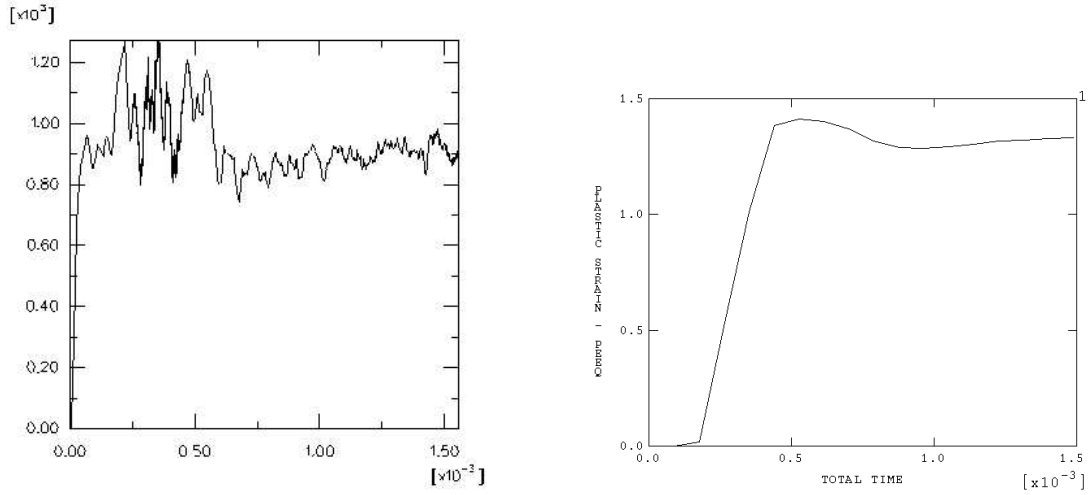

Figure 8: Cutting force evolution (Newton) and Plastic strain evolution for an element in the middle of the chip

thickness of the workpiece is $2\,mm$); in table 4 different values are compared with Joyot [16] and Pantalé [14] numerical results, as well as experimental ones and Oxley (see Pantalé [14] for results using the Oxley model) analytical model results.

	Actual model	Experimental	Joyot model	Pantalé model	Oxley model
$\sigma_{max}(GPa)$	1.03	–	1.4	1.0	–
$T_{max}(°K)$	1350	–	1500	1400	–
$F_c(N)$	1800	1860	1740	2096	2328

Table 4: Results comparisons

4.2 Three-dimensional oblique model results

In this section, we have realized an extension of the two-dimensional model presented before to perform a three-dimensional model of unsteady-state metal cutting. Results of thermo-mechanical values and side-effects have also been observed, and are in agreement with Pantalé [14] results. Finally, a three-dimensional unsteady-state oblique model has been developed and this is the one that we will present here. This model uses the same geometry and cutting parameters as the two-dimensional model described before; we just give an inclination angle of 5° to the tool ($K_r = 85°$). Material and damage laws are the same and this model is formulated in A.L.E. The numerical model is made of 25006 nodes and 30925 brick elements. Chip formation and von Mises stress distributions are presented in figure 9. The evolution of the main component of the cutting force (direction 1) is presented in figure 10.

Cutting force results agree with experimental and two-dimensional models (table 5). We note that the little inclination angle does not modify the stabilized values.

4.3 Numerical model of milling

The use of a fracture criterion as described in previous sections avoids the problem of a predefined fracture line. This allows to model complex tool trajectories and keeps free chip formation. The case of a three dimensional

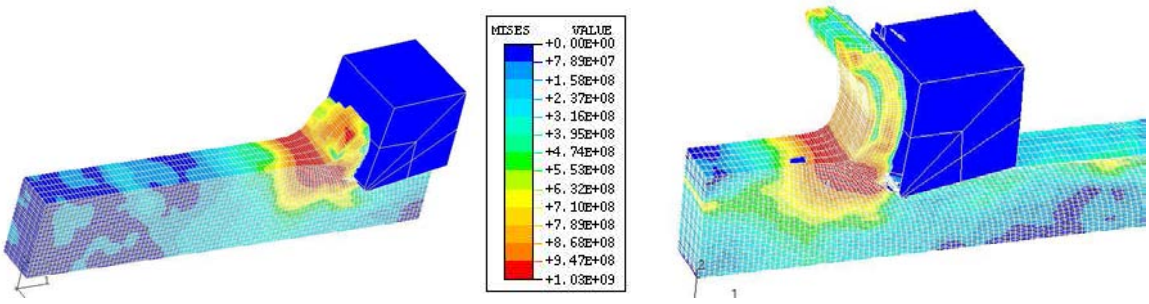

Figure 9: von Mises stresses distribution at time $t = 0.4\,ms$ and time $t = 1.5\,ms$

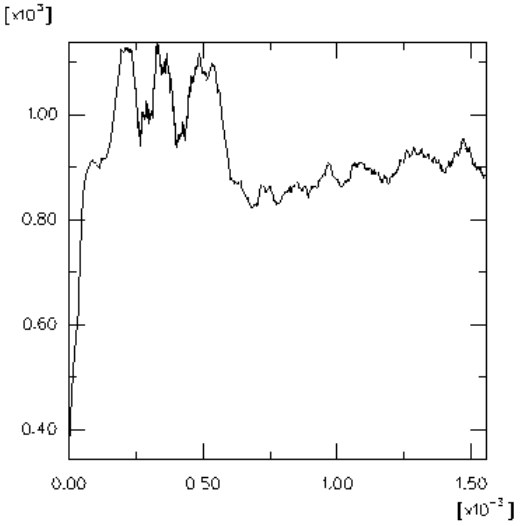

Figure 10: Evolution of the cutting force (component 1)

	2D model	Experimental	Actual model
$\sigma_{max}(GPa)$	1.03	–	1.03
$T_{max}(°K)$	1350	–	1360
$F_c(N)$	1800	1860	1850

Table 5: Comparison of numerical results

milling simulation is so complex that it is impossible to predict fracture node lines and it represents an interesting case for the testing of such a criterion.

The milling operation presented in figure 11 is modeled using a three-dimensional simulation. The tool is considered to be rigid and to move at a rotating velocity $V_r = 120\,rev/min$ and a translating velocity $V_t = 50\,m/s$. The external diameter of the milling cutter is $d = 3mm$, the twist angle is $\alpha = 30°$ and this tool

supports 8 teeth. Only a part of the twist milling cutter has been modeled to reduce the number of elements.

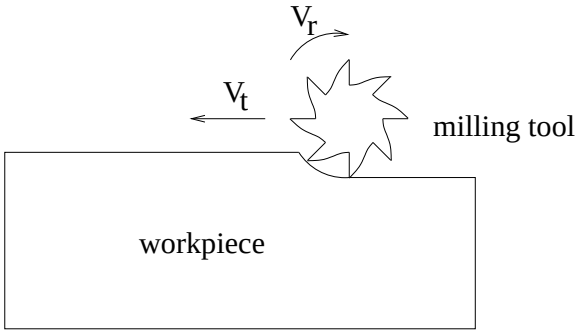

Figure 11: Three-dimensional milling operation

The initial mesh and initial configuration are shown in figure 12. The numerical model is made of 32875 nodes and 30534 brick elements. The total simulation took about 5 hours and required 80000 explicit steps to complete. The results are focused on the third tooth of the milling tool presented in figure 12. In this simulation, the first and second teeth create chips which have geometrical differences from the ones generated by all the next teeth. The third tooth and the following ones generates identical chips because the process becomes a cyclic steady-state one. The results of the von Mises stresses and chip formation are shown at two different stages during the simulation (figure 13).

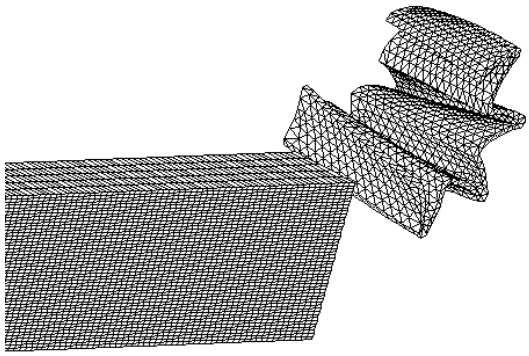

Figure 12: Initial mesh and configuration for the milling simulation

When a tooth of the milling cutter penetrates the workpiece, the primary shear band is clearly visible (left side in figure 13). At this time, the configuration is the same as for an oblique orthogonal metal cutting model. Then, the chip is broken along the primary shear band due to the rotating velocity of the tool and the fracture of the material happens (right side in figure 13). The rupture occurs near the tip of the tool and propagates along the primary shear band to the surface of the chip in contrast to the continuous chip formation where the rupture propagates along a line in front of the tool tip. An instant later, the same tooth comes out of the workpiece and the next tooth enters to machine the next chip. Only one tooth machines the workpiece at a given time during the simulation; this is a cyclic phenomenon which produces segmented chips.

More investigations must be carried out in order to understand each step of the milling operation in studying shear bands and cutting forces.

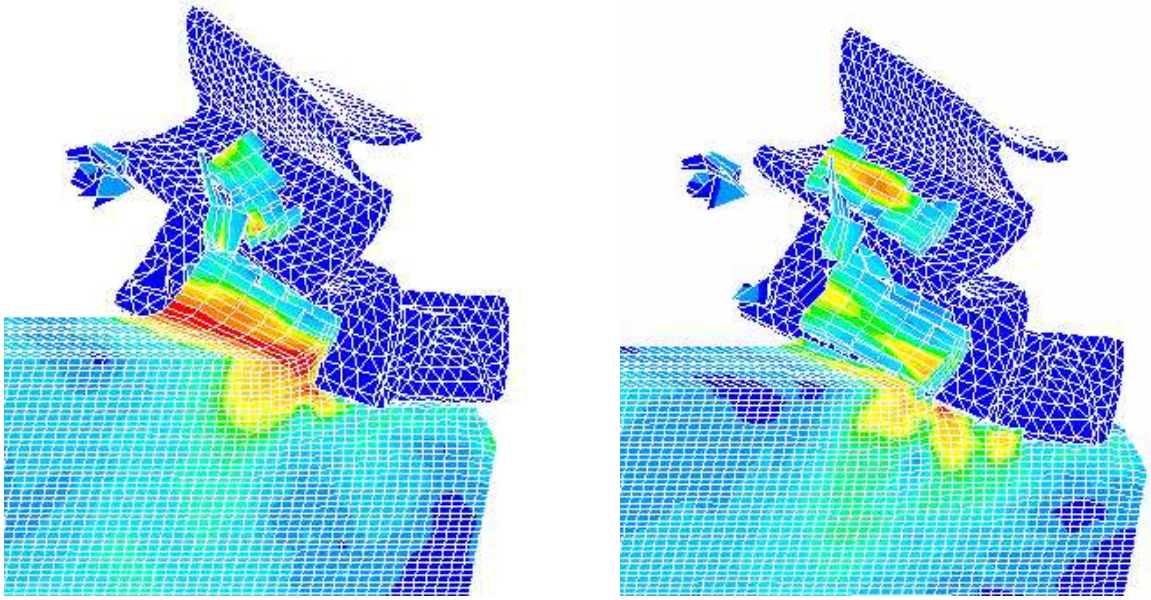

(a) chip formation (b) chip detachment

Figure 13: von Mises stresses distribution for the milling simulation

5 CONCLUSION

In this paper we have presented a complete procedure for the simulation of the cutting operation. Starting from the identification of the constitutive and damage laws of the material, a numerical model is built, for which it must be emphasized that the formation of the chip involves the intrinsic behavior of the material, then bringing a comprehensive model of what is called "machinability". Actual investigations concern the simulation of milling for which the path of the tool tip is not a straight one, and the simulation of sawing for which the tool cannot be considered as a rigid body.

References

[1] A. J. M. Shih, H. T. Y. Yang, and S. Chandrasekar. Experimental and finite element simulation of metal cutting process with strain rate and temperature effects. *Fundamental Issues in Machining, ASME PED*, 43:11–24, 1990.

[2] G. S. Sekhon and J. L. Chenot. Numerical simulation of continuous chip formation during non steady orthogonal cutting. *Engineering computations*, 10:31–48, 1993.

[3] T. Obikawa, H. Sasahara, T. Shirakashi, and E. Usui. Application of computational machining method to discontinuous chip formation. *Journal of Manufacturing Science and Engineering*, 119:667–674, 1997.

[4] J. T. Carrol and J. S. Strenkowski. Finite element models of orthogonal cutting with application to single point diamond turning. *International Journal of Mechanical Sciences*, 30(12):899–920, 1988.

[5] K. Iwata, K. Osakada, and Y. Terasaka. Process modeling of orthogonal cutting by the rigid-plastic finite element method. *Transactions of the ASME*, 106:132–138, 1984.

[6] T. H. C. Childs and K. Maekawa. Computer-aided simulation and experimental studies of chip flow and tool wear in the turning of low alloy steels by cemented carbide tools. *Wear*, 139:235–250, 1990.

[7] Z. C. Lin and S. Y. Lin. A coupled finite element model of thermo-elastic-plastic large deformation for orthogonal cutting. *Journal of Engineering Materials and Technology*, 114(2):218–226, 1992.

[8] J. S. Strenkowski and J. T. Carroll. A finite element model of orthogonal metal cutting. *Journal of Engineering for Industry*, 107:349–354, 1985.

[9] Z. C. Lin and W. C. Pan. A thermoelastic-plastic large deformation model for orthogonal cutting with tool flank wear. i: Computational procedures. *International Journal of Mechanical Sciences*, 35(10):829–840, 1993.

[10] T. D. Marusich and M. Ortiz. Modelling and simulation of high-speed machining. *International Journal for Numerical Methods in Engineering*, 38:3675–3694, 1995.

[11] Lin and Lin. Fundamental modeling for oblique cutting by thermoelastic plastic fem. *International Journal of Mechanical Sciences*, pages 941–965, 1999.

[12] K. Maekawa, T. Nagayama, I. Ohshima, and R. Murata. Finite element simulation of oblique cutting. *Bulletin of the Japan Society of Precision Engineering*, 24(3):221–222, 1990.

[13] K. Ueda and K. Manabe. Rigid-plastic fem analysis of three-dimensional deformation field in chip formation process. *Annals of the CIRP*, 42:35–38, 1993.

[14] O. Pantalé. *Modélisation et Simulation Tridimensionnelles de la Coupe des Métaux.* PhD thesis, school: Université de Bordeaux I, 1996.

[15] R. Rakotomalala, P. Joyot, and M. Touratier. Arbitrary lagrangian-eulerian thermomechanical finite element model of material cutting. *Communications in Numerical Methods in Engineering*, 9:975–987, 1993.

[16] P. Joyot, R. Rakotomalala, and M. Touratier. Modelisation de l'usinage formulée en euler-lagrange arbitraire. *Supplément au journal de physique III*, 3:1141–1144, 1993.

[17] L. Olovsson, L. Nilsson, and K. Simonsson. An ale formulation for the solution of two-dimensional metal cutting problems. *Computers and Structures*, 72:497–507, 1999.

[18] O. Pantalé, R. Rakotomalala, and M. Touratier. An ale three-dimensional model of orthogonal and oblique metal cutting processes. *International Journal of Forming Processes*, 1(3):371–388, 09 1998.

[19] T. J. R. Hughes. *The Finite Element Method; Linear Static and Dynamic Finite Element Analysis.* Prentice Hall, 1987.

[20] A. N. Brooks and T. J. R. Hughes. Streamline upwind/petrov-galerkin formulations for convective dominated flows with particular emphasis on the incompressible navier-stokes equations. *Computer Methods in Applied Mechanics and Engineering*, 32:199–259, 1982.

[21] B. Van Leer. Towards the ultimate conservative difference scheme iv. a new approach to numerical convection. *Journal of Computational Physics*, 23:276–299, 1977.

[22] D. J. Benson. Momentum advection on staggered mesh. *Journal of Computational Physics*, 100(1):143–162, 1992.

[23] R. Johnson and W. K. Cook. A constitutive model and data for metals subjected to large strains high strain rates and high temperatures. *7th International Symposium on Balistics; The Hague*, pages 541–547, 1983.

[24] Abaqus. *Reference Manual.* Hibbitt, Karlsson and Sorensen Inc., 100 Medway Street, Providence, RI, 02906-4402, USA, 1989.

[25] I. Nistor, O. Pantalé, S. Caperaa, and C. Sattouf. Identification of a dynamic viscoplastic flow law using a combined levenberg-marquardt and monte-carlo algorithm. In CIMNE, editor, *VII International Conference on Computational Plasticity, COMPLAS 2003*, Barcelona, 4 2003.

[26] G. R. Johnson and W. H. Cook. Fracture characteristics of three metals subjected to various strains, strain rates, temperatures and pressures. *Engineering Fracture Mechanics*, 21(1):31–48, 1985.

[27] J. W. Hancock and A. C. Mackenzie. On the mechanisms of ductile failure in high-strength steels subjected to multi-axial stress-states. *Journal of the Mechanics and Physics of Solids*, 24:147–169, 1976.

[28] J. Tyson, T. Schmidt, and K. Galanulis. Advanced photogrammetry for robust deformation and strain measurement. In *Proceedings of the 2002 SEM Annual Conference and Exhibition of Experimental and Applied Mechanics*, 2002.

[29] A. J. M. Shih and H. T. Y. Yang. Experimental and finite element predictions of residual stresses due to orthogonal metal cutting. *International Journal for Numerical Methods in Engineering*, 36:1487–1507, 1993.